Chinese Chemical Letters 35 (2024) 109252

Contents lists available at ScienceDirect

Chinese Chemical Letters

journal homepage: www.elsevier.com/locate/cclet

Crystalline carbon nitride with in-plane built-in electric field accelerates carrier separation for excellent photocatalytic hydrogen evolution

Wengao Zeng, Yuchen Dong, Xiaoyuan Ye, Ziying Zhang, Tuo Zhang, Xiangjiu Guan*, Liejin Guo

International Research Center for Renewable Energy, State Key Laboratory of Multiphase Flow in Power Engineering, Xi'an Jiaotong University, Xi'an 710049, China

ARTICLE INFO

Article history:
Received 20 September 2023
Revised 23 October 2023
Accepted 26 October 2023
Available online 30 October 2023

Keywords:
Crystalline carbon nitride
Built-in electric field
Donor-acceptor structure
Photocatalysis
Hydrogen production

ABSTRACT

Achieving a high carrier migration efficiency by constructing built-in electric field is one of the promising approaches for promoting photocatalytic activity. Herein, we have designed a donor-acceptor (D-A) crystalline carbon nitride (APMCN) with 4-amino-2,6-dihydroxypyrimidine (AP) as electron donor, in which the pyrimidine ring was well embedded in the heptazine ring *via* hydrogen-bonding effect during hydrothermal process. The APMCN shows superior charge-transfer due to giant built-in electric field (5.94 times higher than pristine carbon nitride), thereby exhibiting excellent photocatalytic H_2 evolution rate (1350 μmol/h) with a high AQY (62.8%) at 400 nm. Mechanistic analysis based on detailed experimental investigation together with theoretical analysis reveals that the excellent photocatalytic activity is attributed to the promoted charge separation by the giant internal electric field originated from the D–A structure.

The production of hydrogen (H_2) by absorbing solar light through an efficient photocatalyst is an ideal goal of renewable energy conversion [1]. However, the design of stable, efficient and low-cost photocatalysis remains as a huge challenge [2,3]. An ideal photocatalyst contains three important conditions: proper band gap, high carrier mobility and long carrier lifetime, which are currently limited for most semiconductor photocatalysts [4,5]. Recently, conjugated organic materials have attracted great attention due to their abundant element resource, good visible-light absorption, and extensive structural versatility and tunability [6]. Additionally, the diverse chemical bonds and unique chemical groups exhibit excellent advantages, resulting in a wide application in solar energy utilization, especially organic solar cells and photocatalysis [7,8].

To date, many conjugated organic materials have excellent expansion and application in photocatalysis. Among them, the most representative is polymeric carbon nitride (PCN) reported by Wang *et al.* in 2009 [9]. Generally, PCN has two highly symmetrical planar structures: triazine ring and heptazine ring, which is a key reason for insufficient photocatalytic efficiency. In addition, the low carrier-separation rate and weak light-absorption ability are also two other key reasons.

Searching a suitable method to improve the carrier-separation rate and light-absorption capacity of PCN is necessary for achieving efficient photocatalytic performance. In response to this, peer researchers focused on the crystallization of PCN or the introduction of electron transfer media [7,10,11]. Based on this, building a donor-acceptor (D-A) structure in crystalline PCN may be an excellent means to enhance the activity of photocatalytic H_2 production. The built-in electric field is formed between the electron-rich donor and the electron-deficient acceptor due to the potential difference, which would result in facile exciton dissociation. Che *et al.* previously reported a UCN-BI400 D-A structure, achieving a superior photocatalytic H_2 production [12]. Additionally, the introduction of D-A structure will enhance orbital interactions, degree of π-conjugation and the absorption of visible light, which are all conducive to the photocatalytic reaction [13,14]. Lu *et al.* established a TKCN D-A structure, realizing a light response up to 700 nm [15]. It has been proved that the D-A structure can regulate the built-in electric field and energy band of PCN, while most of previous reports focus on direct thermal condensation methods, which are difficult to modulate the in-plane structure of D-A system, thus greatly limiting the charge-separation efficiency.

* Corresponding author.
E-mail address: xj-guan@mail.xjtu.edu.cn (X. Guan).

https://doi.org/10.1016/j.cclet.2023.109252
1001-8417/

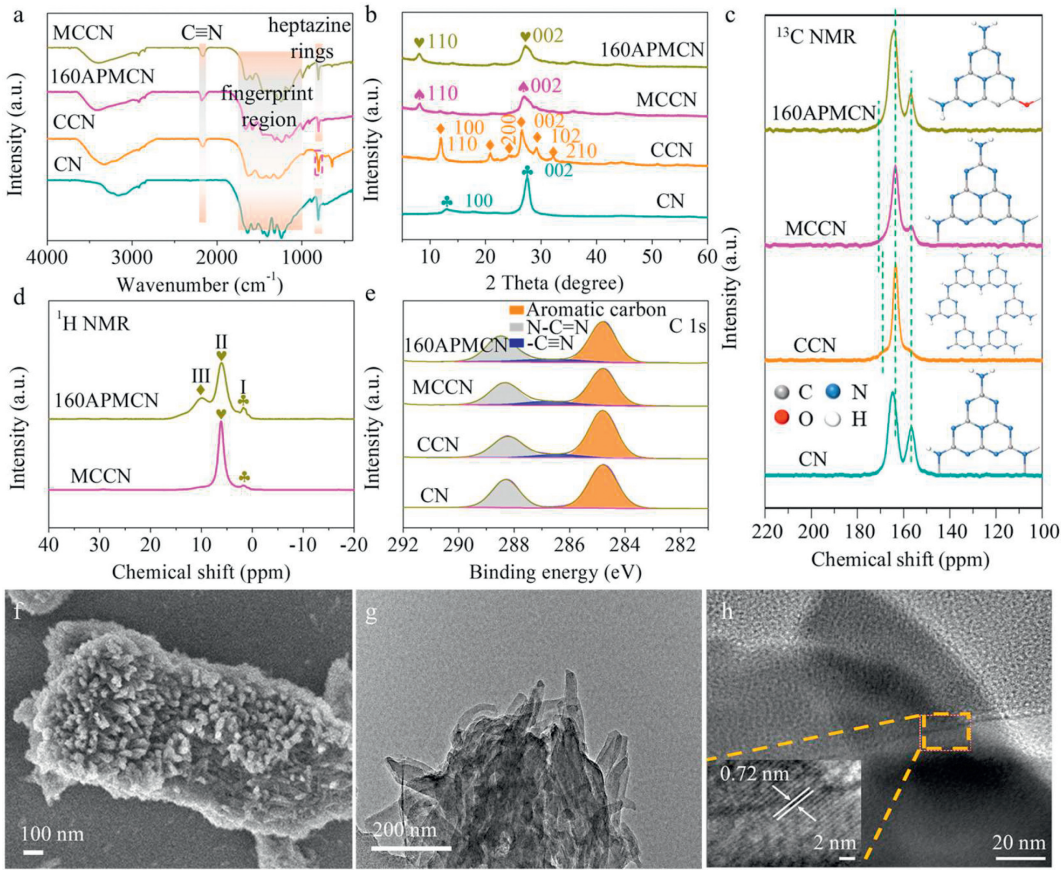

Fig. 1. (a) FT-IR spectrum of CN, CCN, MCCN and 160APMCN. (b) XRD patterns of CN, CCN, MCCN and 160APMCN. (c) ^{13}C NMR of CN, CCN, MCCN and 160APMCN. (d) ^{1}H NMR of CN, CCN, MCCN and 160APMCN. (e) C 1s XPS of CN, CCN, MCCN and 160APMCN. (f) SEM of 160APMCN. (g) TEM of 160APMCN. (h) HRTEM of 160APMCN.

Herein, we have designed a D-A structured crystalline carbon nitride (APMCN) photocatalyst for H_2 production by embedding 4-amino-2,6-dihydroxypyrimidine (AP) as electron donor. Hydroxyl groups in AP could facilitate hydrogen bonds combined with melamine, which could lead to the retention of heptazine ring structure in PCN while retaining the structure stability. Moreover, the unique electron-donating properties of AP embedded in the heptazine ring could help to form an in-plane built-in electric field in D-A structure, thus providing enlarged driving force for the spatial separation of photogenerated charge-carrier.

As shown in Fourier transform infrared (FT-IR) spectra of Figs. S1 and S2 (Supporting information), AP-embedded supermolecules precursor (AMC) and super-molecules precursor (MC) formed relatively strong hydrogen-bond characteristic peak at 2000–3500 cm^{-1}, which indicates the formation of supramolecular structure due to strong hydrogen bond during hydrothermal process [16]. The peak difference of AMC and MC at 2100–3600 cm^{-1} indicates successful synthesis of AP-modified supermolecules. Through the comparison of X-ray diffraction (XRD) patterns (Fig. S3 in Supporting information), it was found that a melamine-cyanuric acid structure was formed and introduction of AP did not change the configuration [16,17]. Subsequently, crystalline carbon nitride (MCCN) was obtained by thermally condensing super-molecules precursors by eutectic salts method. From Fig. 1a, 160APMCN and MCCN contain out-of-plane bending vibration of heptazine rings and ν(C–NH–C) and ν(C≡N) stretching vibrations characteristic peak at 810 cm^{-1} and a fingerprint region between 1200 cm^{-1} and 1700 cm^{-1} [18,19]. Poly(triazine imide) (CCN) contains similar three characteristic peak at 810 cm^{-1} and a fingerprint region between 1200 cm^{-1} and 1700 cm^{-1}, which are attributed to ring sextant out of plane bending, ν(C–NH–C) and ν(C≡N) stretching vibrations respectively [18,19]. Notably, the signal of the heptazine ring is weakened in 160AMC compared to MC due to the introduction of AP. Moreover, by comparing FT-IR spectrum of MC, 160APMCN and 240APMCN (Fig. S4 in Supporting information), it can be found that there is a change between 2500 cm^{-1} and 3650 cm^{-1}, which points to the presence of O–H and C–H. From Fig. 1b, the XRD patterns of APMCN presents a stronger diffraction peak at 28.2° than MCCN, which may be caused by the intercalation of K^+. This could narrow the interlayer distances, facilitating polarization and charge transfer among the neighboring layers. And CNN presents a poly(triazine imide) (PTI) phase [20]. These results show pyrimidine-modified heptazine-based crystalline carbon nitride are successfully synthesized as APMCN.

In addition, nuclear magnetic resonance (NMR) and X-ray photoelectron spectroscopy (XPS) were performed to further define the final structure. From Fig. 1c, the signals of ^{13}C NMR at 165 and 157 ppm can be detected in CN (bulk carbon nitride from direct calculation of melamine), CCN, MCCN and 160APMCN, which attributed to CN_2-(NH_x) and C–N_3 moieties, respectively [21,22]. The peak at 168 ppm may be attributed to C species adjacent to non-protonated ring N atoms. For CCN, the intensity of peak at 157 ppm is weaker than other samples, which suggests CCN is a poly(triazine imide) structure. The characteristic peaks of MCCN and 160APMCN are basically the same, because the sensitivity of ^{13}C NMR is relatively low, and weak changes cannot be detected. Therefore, to demonstrate the intercalation of AP, the ^{1}H NMR is presented in Fig. 1d, in which peak I and peak II represent –NH_x in the carbon nitride structure. 160APMCN exhibits a peak III in

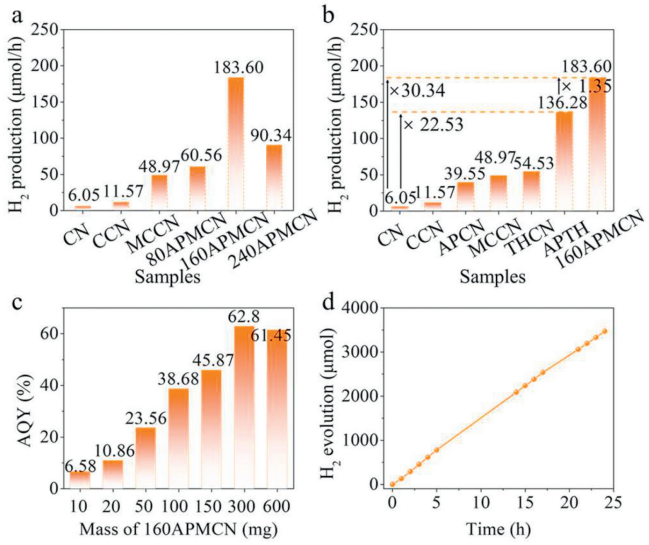

Fig. 2. (a) Hydrogen evolution rate of samples under AM 1.5 G (20 mg, 20%TEOA). (b) Comparison of hydrogen production rates of different samples. (c) The AQY of different mass of 160APMCN (20% TEOA (80 mL), 3% Pt, and 400 nm). (d) Long tests of photocatalytic H_2 production in 160APMCN (20 mg photocatalyst, AM 1.5 G, and 3% Pt).

a relatively large chemical shift, which could be attributed to the –CH introduced by AP intercalation. XPS survey spectrum and inductively coupled plasma mass spectrometer (Fig. S5 and Table S6 in Supporting information) verifies intercalation of K^+ in crystalline carbon nitride, which would improve charge-transfer capacity due to the formation of K^+ bridge [23]. C 1s XPS (Fig. 1e) shows that the crystalline carbon nitride has a weak –C≡N peak signal at 286.4 eV in addition to the N–C=N and aromatic carbon at 288.1 and 284.8 eV compared to CN [24]. Notably, due to the introduction of the pyrimidine ring, both the number of aromatic carbons and C–N=N are increased (Tables S1 and S2 in Supporting information).

Scanning electron microscopy (SEM) and Transmission electron microscopy (TEM) were performed to observe microscopic morphology of samples. CN appears as sheet-assembled bulk of different sizes (Fig. S6a in Supporting information). The morphology of CCN (Fig. S6b in Supporting information) formed by melamine reacting with the eutectic salt did not change greatly, but a large part became bundle-like. However, the super-molecules after the hydrothermal reaction were thermally polycondensation with the eutectic salt to form a stamen-like morphology (Fig. S6c in Supporting information). For 160APMCN (Fig. 1f and Fig. S6d in Supporting information), the embedding of AP makes the morphology size smaller than MCCN. Similar results also appeared on TEM images (Fig. 1g), in which 160APMCN presents a bundle-like stacking structure while CN is a typical lamellar structure. According to HRTEM (Fig. 1h), the lattice fringe of 160APMCN is approximately 0.72 nm, indicating that D-A crystalline carbon nitride is successfully synthesized.

H_2 evolution tests were carried out to evaluate the photocatalytic performance. As shown in Figs. 2a and b and Fig. S7 (Supporting information), after reacting with eutectic salts, the H_2 production rate of CCN and MCCN gradually increased, and was about 1.91 times (11.57 μmol/h) and 8.09 times (48.97 μmol/h) higher than that of CN (6.05 μmol/h), respectively. Notably, after introducing AP on MCCN, the H_2 production activity of APMCN significantly increased. The highest H_2 evolution rate reached 183.6 μmol/h, which was about 30.34 times that of CN. More details can be seen in Fig. S8 (Supporting information). According to the results of Brunner-Emmet-Teller surface area (Fig. S9 and Table S3 in Supporting information), compared with CN (5.9 m^2/g), CCN has the largest specific surface area (49.1 m^2/g), and the specific surface area of MCCN (8.6 m^2/g) and APMCN (12.8 m^2/g) does not change significantly. Thus, the efficient photocatalytic H_2 production rates of CCN and MCCN may be mainly caused by enhancement of carrier separation efficiency. In addition, the O_2 evolution activity and overall water splitting activity were given in Figs. S10 and S11 (Supporting information). 160APMCN also exhibits a better activity. To distinguish the activity of introduced AP in different structures, carbon nitride from thermally condensation reaction with eutectic salts by using precursors with different mass ratios to prepare triazine and triazine-heptazine CN (denoted as APCN, APTH and THCN, the relevant data is in Figs. S12 and S13 (Supporting information). From Fig. 2b and Fig. S14 (Supporting information), the H_2 yield of APCN, THCN and APTH reached 39.55, 54.53 and 136.28 μmol/h, respectively, which is 6.5, 9.0 and 22.53 times than CN. This indicates that introduction of AP in triazine, triazine-heptazine and heptazine can promote catalytic activity, and it also proves that the common modification of D-A structure is most conducive to promoting the evolution of H_2.

In addition, mass of photocatalyst was optimized and the underlined role of sacrificial agent was investigated. From Fig. 2c and Fig. S15a (Supporting information), when the catalyst amount reaches 300 mg, the highest hydrogen production can be achieved, reaching 1350 μmol/h. The corresponding AQY at 400 nm can reach 62.8%. Compared with other sacrificial agent (Fig. S15a), the photocatalytic H_2 production exhibits higher in triethanolamine (TEOA). According to Fig. S15c and Table S4 (Supporting information), APMCN still has good photocatalytic performance under illumination of $\lambda > 500$ nm, which is because the supramolecular structure after hydrothermal has a higher conjugation. Meanwhile, the sustained hydrogen production capability of APMCN was evaluated by multiple cycle and 24 h long tests hydrogen production experiments (Fig. 2d and Fig. S15d in Supporting information). After four cycles or 24 h long tests, the activity of APMCN still remained high photocatalytic activity, which indicated that APMCN maintained a good stability. Finally, we also compared the photocatalytic H_2 production activity of 160APMCN and other recently reported crystalline carbon nitride-based materials (Table S7 in Supporting information). 160APMCN exhibits an excellent performance with a relatively high H_2 production activity.

In view of the excellent performance of the photocatalyst, investigation on the factors affecting the activity is further conducted. An ideal photocatalyst needs a strong light absorption capacity, based on which a higher solar energy conversion efficiency could be possible [25,26]. As shown in Fig. 3a and Fig. S16 (Supporting information), the light absorption ability of heptazine-based crystalline carbon nitride generated by the reaction of supramolecular precursors is significantly enhanced. Due to the formation of super-molecules, the enhancement of conjugation degree in MCCN and APMCN make their absorption band edges redshifted [16,27,28]. Similarly, this also explains why 160APMCN has stronger UV absorption ability than MCCN. The band edges of MCCN and 160APMCN are basically unchanged, because AP embedding does not significantly increase the C/N ratio of APMCN. In addition, the energy band positions of catalysts are also crucial in photocatalytic reactions. According to the Mott-Schottky plots (Fig. S17 in Supporting information), the slope of samples is positive, which demonstrate the n-type semiconductor characteristics of samples. For n-type semiconductors, the potential of conduction band minimum (CBM) is approximately equal to the as-estimated flat-band potential [29]. Thus, CBM potential of CN, CCN, MCCN and 160APMCN can be obtained. 160APMCN has a more positive CB (−0.83 eV), which could greatly increase electron transmission kinetics. Therefore, combining UV–vis and Mott-Schottky, a com-

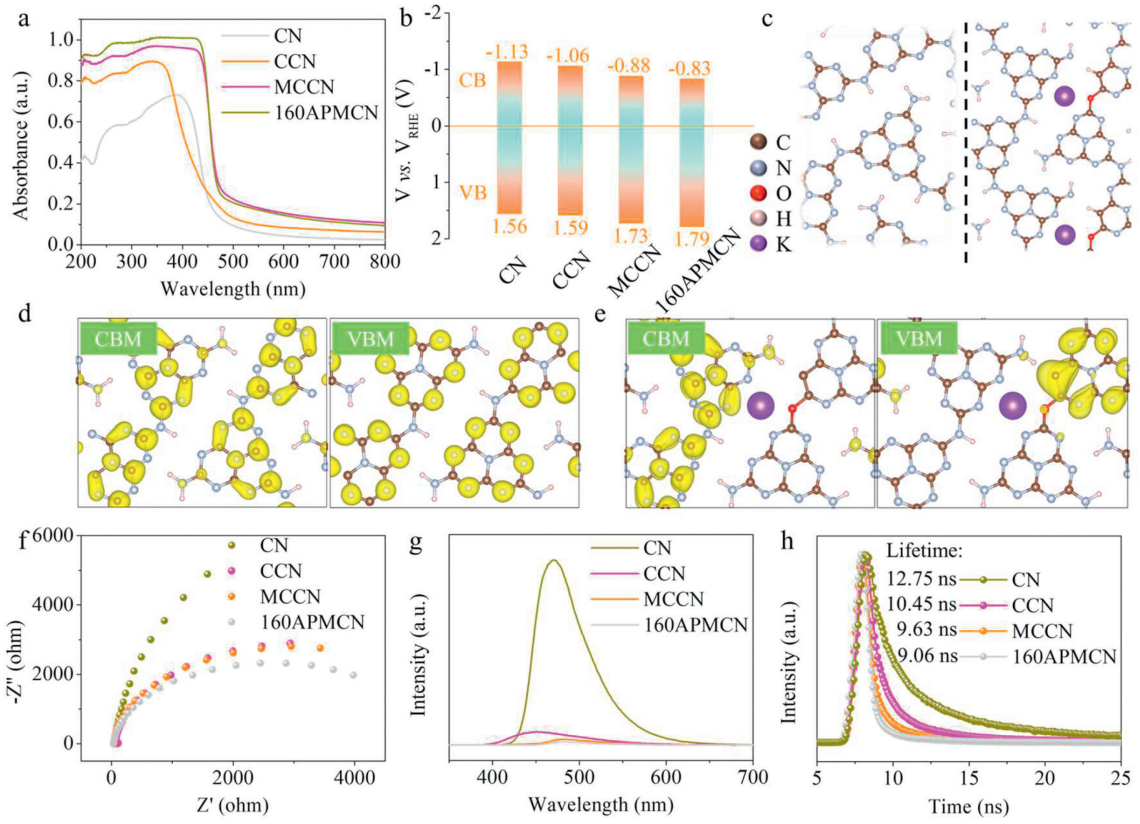

Fig. 3. (a) UV–vis spectra and (b) band positions of CN, CCN, MCCN and 160APMCN. (c) Geometric structures of CN (left) and APMCN (right). (d, e) The VBM and CBM states of CN and APMCN. (f) Electrochemical impedance spectroscopy, (g) steady-state PL spectra and (h) TR-PL of CN, CCN, MCCN and 160APMCN.

parison of the band structures of the samples here is given in Fig. 3b. In addition, first principle calculation based on the density functional theory (DFT) was carried out. The model structure is shown in Fig. 3c, and more details can be found in Fig. S18 (Supporting information). According to the energy band structure and density of states in Fig. S18, the introduction of AP makes more intermediate energy levels appear in both conduction band and valence band of APMCN. Besides the C 2p and N 2p orbitals, O 2p orbitals appear in both the conduction and valence bands of APMCN, which are attributed to the intercalation of AP and the eutectic salt reaction, while K^+ ions are not directly involved in the formation of band edge electric states. In addition, the establishment of the D-A system makes the valence band maximum (VBM) and CBM state distributions in APMCN more dispersed and localized on different melon chains. Specifically, VBM is mainly distributed around pyrimidine-ring, while CBM is located on melon chains without pyrimidine-ring (Figs. 3d and e).

Electrochemical impedance spectroscopy (EIS), fluorescence emission and time-resolved photoluminescence (TR-PL) were carried out to investigate the behavior of photogenerated carriers. For EIS, it represents the charge transfer resistance of catalysts. The smaller the radius of arc, the smaller the resistance. Obviously, the arc radius of 160APMCN is smallest among samples (Fig. 3f), indicating introduction of AP is beneficial to reduce the charge transfer resistance [30]. The decreased charge transfer resistance is positive for charge transfer of catalysts. The fluorescence emission intensity is determined by the electron-hole pair recombination, and the stronger the recombination, the greater the intensity. As shown in Fig. 3g, the highly symmetrical structure of CN seriously hampers its internal charge transfer, so that an obvious fluorescence signal at 470 nm is found. By thermal condensation with eutectic salts, the formation of poly(triazine amide) structure and the high crystallinity can alleviate the carries separation efficiency to a certain extent, hence the signal intensity of CCN decreases [18,31,32]. In addition, the signal intensities of MCCN and 160APMCN are weak, which shows that replacing melamine with super-molecular precursors and thermal polycondensation of eutectic salts further enhances the carrier migration due to the increased degree of conjugation and the complexity of the molecular structure. The signal intensity of 160APMCN is weaker than MCCN, which is mainly ascribe to the formation of D-A structure upon introducing AP, leading to the accelerated separation of carriers. Finally, the TR-PL was carried out (Fig. 3h). Generally, TR-PL was used to study the transport and quenching mechanism of photogenerated excitons. The average fluorescence lifetime represents the time it takes for an exciton to fall from an excited state to a steady state after stopping excitation [16]. The average fluorescence lifetime of CN, CCN, MCCN and 160APMCN are 12.82, 10.46, 9.63 and 9.06 ns, respectively, suggesting that the electron transport ability of APMCN is stronger than CN. More detailed data can be found in Table S8 (Supporting information).

For carries separation, kinetic factors are another very important point. From the electron distribution diagram in Fig. 4a, it can be seen that the introduction of the pyridine ring makes the electron cloud more concentrated on the C atom on the pyridine ring, which results in a potential difference in the melon chain with or without pyrimidine rings. Such distinct electron densities at different sites can induce the generation of built-in electric field between the melon chains with or without pyrimidine rings. According to the plane charge density calculated in Fig. 4b, APMCN has a larger difference between positive and negative charge densities, which can roughly be assumed that APMCN has a larger built-in electric field intensity. Moreover, the built-in electric field intensity is positively depended on the zeta potential and the sur-

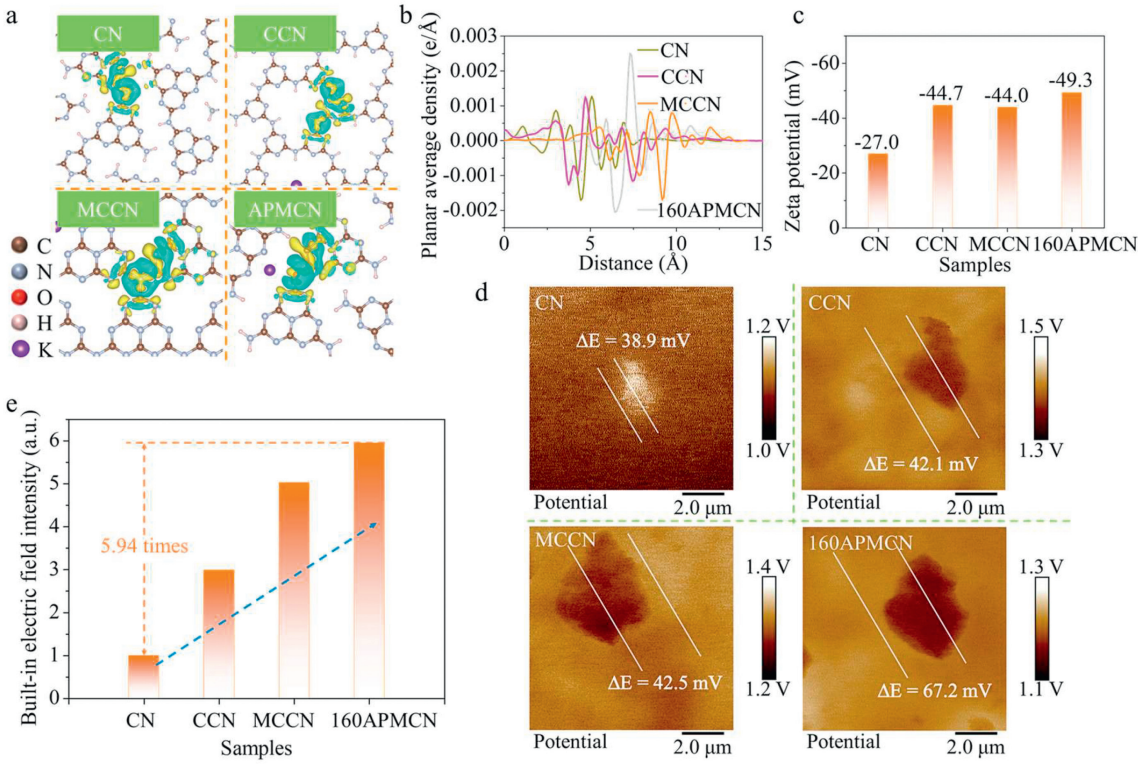

Fig. 4. (a) The electrostatic potential distribution of CN, CCN, MCCN and APMCN. (b) The planar average density (e/Å) of CN, CCN, MCCN and APMCN. (c) The zeta potential of CN, CCN, MCCN and 160APMCN. (d) The surface potential and (e) the built-in electric field intensity of CN, CCN, MCCN and 160APMCN.

face potential [33,34]. As shown in Fig. 4c and Table S5 (Supporting information), the absolute value of APMCN zeta potential (−49.3 mV) is the largest than the rest of the samples (CN: −27 mV; CCN: −44.7 mV and MCCN: −44.0 mV). And according to the surface potential measured by atomic force microscopy with a Kelvin probe (Fig. 4d), it can be seen that the surface potential of APMCN ($\Delta E = 67.2$ mV) is higher than that of CN ($\Delta E = 38.9$ mV) and MCCN ($\Delta E = 42.5$ mV). The corresponding potential curve is provided in Fig. S19 (Supporting information). Besides, molecular dipole moment is also an important factor affecting the strength of the built-in electric field [14]. As shown in Fig. S20 (Supporting information), the dipole of APMCN is 13.46 Debye, which is much larger than that of MCCN (6.49 Debye) and CN (0.26 Debye). The larger molecular dipole of the D–A system ensures a large enough built-in electric field, which benefits the photoinduced carrier separation. As a result, the stronger built-in electric field of D–A catalyst APMCN significantly enhanced the carries separation and transportation. Furthermore, based the surface photovoltage intensity (Fig. S21 in Supporting information) [35,36], it can be quantificationally obtained that the internal electric field intensity of APMCN is 5.94 times as high as that of CN (Fig. 4e) [14,37]. Beyond that, it is well known that the built-in electric field is closely related to the dissociation of exciton. The key factor of exciton dissociation is exciton binding energy (E_b) [38–40]. As shown in Fig. S22 (Supporting information), the temperature-dependent photoluminescence was used to evaluate exciton dissociation behavior. The increased temperature promotes the dissociation of excitons, which means that there are more free carriers and a decrease in PL intensity. The E_b of APMCN is the lowest of all samples, only 21.4 meV (CN: 32.2 meV, CCN: 24.4 meV, MCCN: 21.7 meV). This result indicates that excitons of APMCN accelerated dissociation due to the formation of giant built-in electric field. As a result, more free carriers are available to participate in redox reactions, thereby promoting photocatalytic hydrogen production.

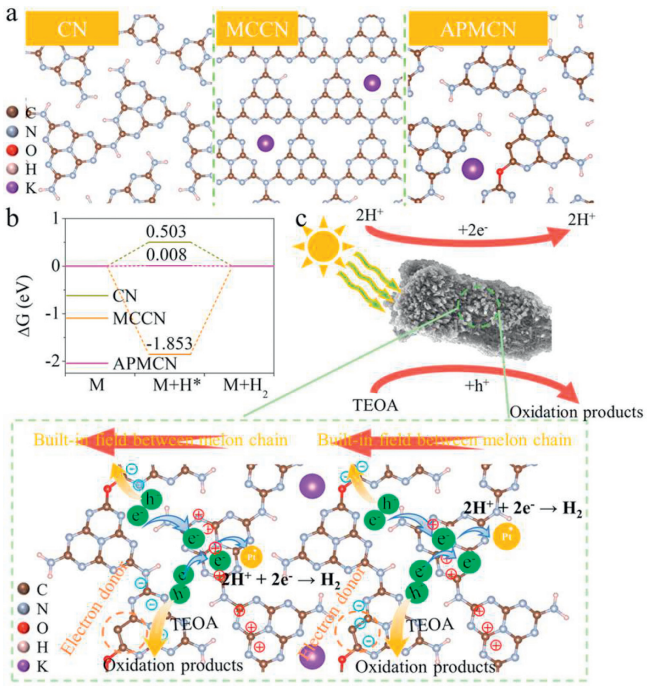

Fig. 5. (a) The optimized geometric structures and (b) Free energy diagram for photocatalytic H_2 production of CN, MCCN and APMCN. (c) A schematic illustration involved in the photocatalytic H_2 production process of APMCN.

Finally, in order to understand the reaction mechanism of APMCN, the free energy during photocatalytic H_2 production was calculated. Fig. 5a gives the optimized geometric structures, in which it can be seen that the H* adsorption all occurs on the C

atoms. The free energy of photocatalytic H_2 production is given in Fig. 5b. The free energy of CN (0.503 eV) changes a little, but it is a relatively large positive value, which indicates that H atoms are difficult to be adsorbed [23]. For MCCN, the free energy is −1.853 eV, H atoms can be easily adsorbed on C atoms, but due to too low free energy, it is difficult for H^* to desorb to form H_2. After the introduction of AP, it can be found that the free energy change of APMCN is the smallest, and the value (0.008) is close to 0, suggesting that the H^* adsorption process of APMCN and the process of H^* to H_2 are easy to proceed. This should also be one of the important reasons for the high activity of APMCN.

According to all the above analysis, photocatalytic mechanism of APMCN is given in Fig. 5c. After APMCN was excited by simulated sunlight, photogenerated electron pairs were generated. The construction of the D-A system results in a significant potential difference (AP as a donor) between different melon chains in APMCN, forming an electric field directed towards the melon chain with a pyrimidine ring. Under the action of an electric field, not only does it accelerate the migration of charge carriers, but it also causes spatial separation of charge carriers, greatly promoting the utilization efficiency of charge carriers. Finally, the electrons and holes reach the reaction sites respectively, the electrons react with the adsorbed H atoms to generate H_2, and the holes react with TEOA to generate the corresponding oxidation products.

In summary, the heptazine-based D-A structure crystalline carbon nitride was achieved by introducing electron donor *via* a method of super-molecules precursor route. An in-plane built-in electric field was formed *via* AP embedding in heptazine ring, which promises a higher charge-separation efficiency in as-prepared APMCN photocatalyst. Comprehensive characterization combined with theoretical analysis demonstrate the established strong in-plane built-in electric field and the accelerated charge-separation. As a result, efficient photocatalytic H_2 production is achieved, which is a more decent level than many reported crystalline carbon nitride materials. Overall, this work provided a new route to design high-activity photocatalyst *via* constructing in-plane electric field, which is helpful for the development of designing D-A materials to clean energy production.

Declaration of competing interest

The authors declare that they have no known competing financial interests or personal relationships that could have appeared to influence the work reported in this paper.

Acknowledgments

This work is supported by the Basic Science Center Program for Ordered Energy Conversion of the National Natural Science Foundation of China (No. 51888103), the National Natural Science Foundation of China (Nos. 52376209 and 52172248), China Postdoctoral Science Foundation (Nos. 2020M673386 and 2020T130503), and China Fundamental Research Funds for the Central Universities.

Supplementary materials

Supplementary material associated with this article can be found, in the online version, at doi:10.1016/j.cclet.2023.109252.

References

[1] G. Lin, X. Sun, X. Xu, Appl. Catal. B: Environ. 324 (2023) 122258.
[2] L. Xie, L. Wang, W. Zhao, et al., Nat. Commun. 12 (2021) 5070.
[3] Y. Zhang, S. Zhan, K. Liu, et al., Angew. Chem. Int. Ed. 62 (2022) e202217191.
[4] T. Cai, W. Zeng, Y. Liu, et al., Appl. Catal. B: Environ. 263 (2020) 118327.
[5] Z. Yang, X. Xia, W. Yang, L. Wang, Y. Liu, Appl. Catal. B: Environ. 299 (2021) 120675.
[6] C. Dai, B. Liu, Energy Environ. Sci. 13 (2020) 24–52.
[7] Z.A. Lan, M. Wu, Z.P. Fang, et al., Angew. Chem. Int. Ed. 60 (2021) 16355–16359.
[8] M. Liu, C. Wei, H. Zhuzhang, et al., Angew. Chem. Int. Ed. 61 (2022) e202113389.
[9] X. Wang, K. Maeda, A. Thomas, et al., Nat. Mater. 8 (2009) 76–80.
[10] H. Hou, G. Shao, W. Yang, J. Mater. Chem. A 9 (2021) 13722–13745.
[11] C. Wang, H. Zhang, W. Luo, T. Sun, Y. Xu, Angew. Chem. Int. Ed. 60 (2021) 25381–25390.
[12] H. Che, C. Li, C. Li, et al., Chem. Eng. J. 410 (2021) 127791.
[13] S. Barman, A. Singh, F.A. Rahimi, T.K. Maji, J. Am. Chem. Soc. 143 (2021) 16284–16292.
[14] J. Yang, J. Jing, Y. Zhu, Adv. Mater. 33 (2021) 2101026.
[15] G. Zhang, Y. Xu, H. Mi, et al., ChemSusChem 14 (2021) 4516–4524.
[16] B. Wu, L. Zhang, B. Jiang, et al., Angew. Chem. Int. Ed. 60 (2021) 4815–4822.
[17] J. Chen, C.L. Dong, D. Zhao, et al., Adv. Mater. 29 (2017) 1606198.
[18] L. Lin, Z. Yu, X. Wang, Angew. Chem. Int. Ed. 58 (2019) 6164–6175.
[19] Z. Zhai, H. Zhang, F. Niu, et al., ACS Nano 16 (2022) 21002–21012.
[20] K. Schwinghammer, B. Tuffy, M.B. Mesch, et al., Angew. Chem. Int. Ed. 52 (2013) 2435–2439.
[21] X. Zhang, P. Ma, C. Wang, et al., Energy Environ. Sci. 15 (2022) 830–842.
[22] D. Zhao, C.L. Dong, W. Bin, et al., Adv. Mater. 31 (2019) 1903545.
[23] B.B. Xu, X.B. Fu, X. You, et al., ACS Catal. 12 (2022) 6958–6967.
[24] G. Zhang, J. Zhu, Y. Xu, et al., ACS Catal. 12 (2022) 4648–4658.
[25] X. Sun, S. Jiang, H. Huang, et al., Angew. Chem. Int. Ed. 61 (2022) e202204880.
[26] Z. Wang, C. Li, K. Domen, Chem. Soc. Rev. 48 (2019) 2109–2125.
[27] H. Che, C. Liu, G. Che, et al., Nano Energy 67 (2020) 104273.
[28] H. Li, F. Li, Z. Wang, et al., Appl. Catal. B: Environ. 229 (2018) 114–120.
[29] Q. Yang, T. Wang, Z. Zheng, et al., Appl. Catal. B: Environ. 315 (2022) 121575.
[30] H. Niu, W. Zhao, H. Lv, Y. Yang, Y. Cai, Chem. Eng. J. 411 (2021) 128400.
[31] M. Liu, C. Wei, H. Zhuzhang, et al., Angew. Chem. Int. Ed. 61 (2021) e202113389.
[32] G. Zhang, L. Lin, G. Li, et al., Angew. Chem. Int. Ed. 57 (2018) 9372–9376.
[33] J. Jing, J. Yang, W. Li, Z. Wu, Y. Zhu, Adv. Mater. 34 (2022) 2106807.
[34] J. Jing, J. Yang, Z. Zhang, Y. Zhu, Adv. Energy Mater. 11 (2021) 2101392.
[35] T. Kanata, M. Matsunaga, H. Takakura, Y. Hamakawa, T. Nishino, Proc. SPIE-Int. Soc. Opt. Eng. 1286 (1990) 56–65.
[36] G. Morello, F.D. Sala, L. Carbone, et al., Phys. Rev. B 78 (2008) 195313.
[37] Y. Sheng, W. Li, L. Xu, Y. Zhu, Adv. Mater. 34 (2022) 2102354.
[38] Z.A. Lan, G. Zhang, X. Chen, et al., Angew. Chem. Int. Ed. 58 (2019) 10236–10240.
[39] H. Wang, S. Jin, X. Zhang, Y. Xie, Angew. Chem. Int. Ed. 59 (2020) 22828–22839.
[40] H. Wang, W. Liu, X. He, et al., J. Am. Chem. Soc. 142 (2020) 14007–14022.